Macromolecules

pubs.acs.org/Macromolecules Article

Dynamics of Polymerization and Gelation in Epoxy Nanocomposites *via* X-ray Photon Correlation Spectroscopy

Edward B. Trigg, Lutz Wiegart, Andrei Fluerasu, and Hilmar Koerner*

Cite This: *Macromolecules* 2021, 54, 6575−6584 Read Online

ACCESS | Metrics & More | Article Recommendations | Supporting Information

ABSTRACT: The details of the curing process of epoxy resins are notoriously difficult to ascertain, hampering polymer matrix composite manufacturing. Here, the curing of a series of six epoxy resins containing dilute spherical nanoparticles was investigated *via* X-ray photon correlation spectroscopy (XPCS). The resin formulation was varied to achieve a range of crosslink densities and topologies. Prior to gelation, the viscosities obtained from XPCS agreed with bulk rheology. A clear dynamic transition was detected in all samples, where the q-scaling changes from approximately $q^{2.2}$ to q^{1}, indicating a transition from sub-diffusive to ballistic-like nanoparticle motion. For the samples with a high crosslink density, this change was abrupt and coincided with gelation, and there was no evidence of crosslink heterogeneity. Chain entanglement played a role in the transition for samples with lower crosslink density. This work reveals the potential of XPCS to deliver new quantitative insights into the curing process of thermosetting resins.

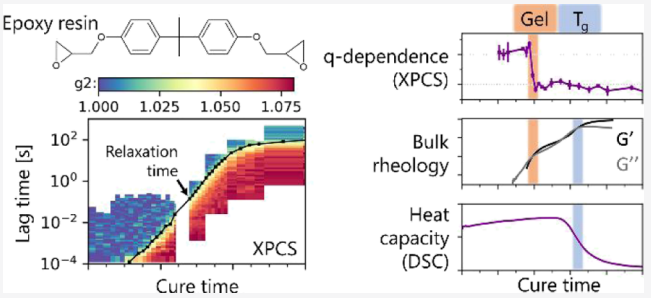

INTRODUCTION

Epoxy resins are among the most widely used thermosets, with important applications in carbon fiber composites, aerospace, and electronics. Despite decades of academic research and widespread industrial use, aspects of the curing process of epoxies are still somewhat mysterious, and an improved fundamental understanding of their nanoscale details could yield substantial improvements in manufacturing processes and macroscopic properties. For instance, it is well known that their final properties depend on curing conditions,[1−7] but in the absence of a definitive theoretical framework to explain this path-dependence, industrial processes are typically optimized by trial and error and lead to empirically derived cure cycles that are conservative and time-consuming.

A significant challenge in understanding epoxy resins is the difficulty in probing the network formation and topology during cure. Traditionally, researchers applied techniques such as bulk rheology and dielectric spectroscopy.[8,9] While valuable in many ways, these techniques have important limitations. Rheology only probes the bulk response of the material and is often ill-suited to elucidate heterogeneities, which are currently thought to be a primary factor in performance optimization.[10,11] Dielectric spectroscopy probes extremely localized dynamics on the order of several chemical bonds, and information about larger length scales is difficult to extract.

Meanwhile, morphological characterization results of cured resins have suggested that the resins can be heterogeneous at length scales of 10s to 1000s of nanometers. The heterogeneity, often attributed to variations in crosslink density, is usually seen after cure via surface-sensitive techniques such as atomic force microscopy (AFM)[12,13] and scanning electron microscopy.[14] Chemical heterogeneities have also been reported via AFM−infrared spectroscopy,[15,16] and single-particle tracking in a dilute epoxy nanocomposite suggested dynamic heterogeneity in the resin during cure.[17] However, other researchers have cast doubt on the idea of network heterogeneity.[18,19] This controversy speaks of the great difficulty in probing the topology of the crosslink network in epoxy resins; many techniques leave speculative conclusions at best.

Here, we perform *in situ* X-ray photon correlation spectroscopy (XPCS) on epoxy resins during cure. XPCS probes the nanoscale dynamics in bulk samples by measuring the correlation function of scattered coherent X-rays.[20,21] By doing so at a variety of wavevectors (q), dynamics over a range of length scales, here 20−100 nm, are probed. Dilute spherical nanoparticles (NPs) were added to the resin at a concentration of 1 vol % to serve as probes, as this neat resin is not suitable for XPCS due to low small-angle X-ray scattering intensity. The microrheology theory quantitatively relates the (quasi-) equilibrium dynamics of an ensemble of non-interacting particles to their matrix.[22] XPCS is particularly well-suited

Received: April 1, 2021
Revised: June 3, 2021
Published: June 17, 2021

https://doi.org/10.1021/acs.macromol.1c00727
Macromolecules 2021, 54, 6575−6584

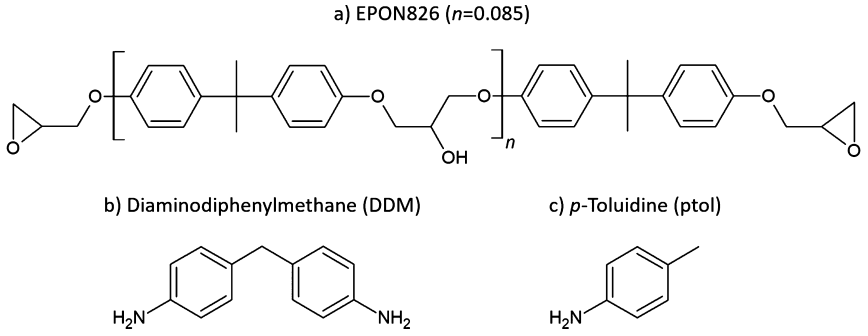

Figure 1. Chemical structures of monomers used: (a) EPON826, a commercial epoxy based on diglycidyl ether bisphenol A (n = 0.085), (b) DDM, and (c) ptol.

Table 1. Samples Used for This Study; All Contain 1 vol % NPs

sample name	ptol concentration [mol/mol EPON826]	DDM concentration [mol/mol EPON826]	theoretical volumetric crosslink density [nm^{-3}][a]	average molecular weight between crosslinks [Da][a]
ptol-0%	0.00	0.50	0.75	340
ptol-50%	0.50	0.25	0.37	880
ptol-75%	0.75	0.125	0.19	1960
ptol-90%	0.90	0.05	0.07	5200
ptol-95%	0.95	0.025	0.04	10,600
ptol-100%	1.00	0.00	0	∞

[a]Calculated for the fully cured system, assuming that every DDM molecule acts as a crosslink, no etherification occurs, and density = 1.1 g/cm^3.

for these *in situ* experiments because (i) it is non-destructive (if appropriate precautions are taken to avoid beam damage), (ii) it does not perturb the system, and (iii) data are often acquired rapidly (seconds to minutes). Another advantage of XPCS is that it probes bulk volumes of the sample—here, $>10^6$ μm^3, or $>10^{10}$ NPs—so the data reflect the average dynamics throughout the material. A previous study reported XPCS on an industrial composite consisting of epoxy resin heavily loaded with 2 μm particles (25 wt %) as well as micron-scale platelets (1.5 wt %).[23] Due to the large, non-uniformly shaped, highly loaded particles, quantitative information about the resin was not accessible. With our approach—using dilute, 15 nm NPs—we use the microrheology theory to obtain quantitative rheological information as well as observe a distinct dynamic transition upon gelation.

EPON826, an industrial monomer based on diglycidyl ether bisphenol A, was selected for the epoxide. EPON826 contains a small population of dimers (Figure 1a), which retards crystallization of the monomer. For the NPs, 15 nm silica particles (Nissan Chemical) were used. These NPs disperse readily in epoxy resin and are nonreactive according to the manufacturer. To vary the crosslink density, the difunctional and monofunctional amines diaminodiphenylmethane (DDM) and *para*-toluidine (ptol) were selected as curing agents (Figure 1b,c). By varying the ratio of DDM to ptol while maintaining a 1:1 stoichiometry with the epoxide, the crosslinking density can be varied over a broad range (see Table 1). These curing agents are particularly advantageous because (i) they have been shown to exhibit similar reaction kinetics,[24] (ii) they react very slowly at room temperature, simplifying sample preparation, and (iii) the curing reaction approaches completion after about 2 h at the relatively low temperature of 110 °C, streamlining the *in situ* curing experiments at the beamline. We found that the reaction kinetics at 110 °C are slow enough to be captured appropriately by XPCS.

MATERIALS AND METHODS

Materials. EPON826 was purchased from Hexion (Columbus, OH). DDM and ptol were purchased from Sigma-Aldrich. Their chemical structures are shown in Figure 1. Silica NPs were purchased from Nissan Chemical (part number MEK-EC-2130Y). The NPs were nominally spherical with a diameter of 15.5 ± 5.7 nm (Figure S1), which were obtained as dispersed in methyl ethyl ketone (MEK) at 30 wt % and are non-reactive in epoxy resins according to the manufacturer.

Sample Preparation. To make resin formulations, the NPs were first dispersed in EPON826. 20.2 g of EPON826 was dissolved in 21 mL of MEK in a round-bottom flask, and 1.35 g of the as-received NP suspension was added to the EPON826 solution. The mixture was stirred and then placed in a rotary evaporator at 60 °C to remove the MEK. Residual MEK was removed completely under vacuum (<10 mbar) for 3 days at 40 °C and confirmed by the disappearance of the carbonyl stretch in the FTIR spectrum.

The amines were added to the epoxy using a procedure similar to that of Blanco *et al.*[24] To dissolve the DDM in the EPON826-NP colloidal suspension, the DDM was ground to a fine powder by a mortar and pestle. 6.31 g of EPON826-NP was transferred to a glass vial and was stirred vigorously in an oil bath set to 80 °C. 1.68 g of DDM powder was added. The stirring continued for 10 min until the powder was dissolved, and then the mixture was quenched in ice. ptol was added to another portion of the EPON826-NP using the same procedure but with the oil bath set to 50 °C instead of 80 °C, and dissolving took 6 min instead of 10. Negligible reaction occurred during these mixing steps, as shown by nuclear magnetic resonance (NMR) spectroscopy (Figure S2). To make the samples containing different ratios of DDM and ptol, the two resins (EPON826-NP-DDM and EPON826-NP-ptol) were combined in appropriate ratios and stirred with a spatula for 1 min. After mixing, all samples were stored in a −85 °C freezer or on dry ice. The composition of each sample is listed in Table 1.

XPCS Experiments. XPCS was performed at the beamline 11-ID (CHX) at the National Synchrotron Light Source II (NSLS-II). The partially coherent X-rays had an energy of 9.65 keV (wavelength λ = 1.2847 Å) defined by a double crystal monochromator using Si111 reflections. The beam diameter at the sample was approximately 45 μm, defined by a set of high precision slits combined with focusing in

https://doi.org/10.1021/acs.macromol.1c00727
Macromolecules 2021, 54, 6575−6584

the vertical direction using compound refractive lenses. Two detectors, located 10.08 m downstream of the sample, were used sequentially for each *in situ* curing experiment: at the early stages of cure, an Eiger X 500k (Dectris) collected partially coherent small-angle X-ray scattering patterns at a frame rate of 9 kHz, and during the experiment, it was exchanged (via motorized stages) for an Eiger X 4M (Dectris) detector. The latter has a maximum frame rate limited to 750 Hz, but due to its larger size, it gives access to a larger wavevector q, where $q = 4\pi \cdot \sin(\theta)/\lambda$ with the scattering angle 2θ.

The samples were shipped to NSLS-II on dry ice and upon arrival were transferred to a freezer set to −80 °C. Immediately prior to an experiment, a sample vial was removed from refrigeration, allowed to warm to room temperature, and some sample was loaded via a spatula into a custom-built aluminum cell with Kapton windows sealed tightly with O-rings. The cell was inserted into the beamline's hot stage and heated at a rate of 5 °C/min to 110 °C. When the sample reached 110 °C, XPCS data collection began.

Initially, the frame rate was 9 kHz and 10,000 frames were collected for each data set. The frame rate was progressively reduced over time to track the NP dynamics, which decrease as the cure reaction takes place. For frame rates below 9 kHz, the number of frames per data set was 1000. The slowest frame rate was 0.32 Hz. After each set of frames was collected, the sample position was shifted by 75 μm to avoid beam damage. When the frame rate was reduced, the X-ray beam was attenuated with double-sided polished silicon wafers so that for each data set the dose on the sample was kept constant. We confirmed that there was no detectable beam damage by running ptol-90% with half the dose, Figure S3.

XPCS Analysis. For the analysis of the XPCS data, we calculated the time-resolved two-time correlation functions for sets of distinct q values[25] using a Python-based code available at the CHX beamline.[26] However, we found that the two-time correlation functions were generally quasi-stationary over the measurement time, so the corresponding time-averaged one-time correlation functions $g_2(\tau)$ are analyzed herein. The number of q values with high-quality g_2 data varied, so for each data set, the data were manually inspected to select q values where g_2 could be reasonably fit. The selected g_2 functions were fit with a single compressed exponential function[27]

$$g_2(\tau, q) = \beta \exp[-(\Gamma(q)\tau)^{\gamma}] + g_{\infty} \quad (1)$$

where β is the setup-dependent contrast factor, Γ is the q-dependent relaxation rate, τ is the delay time, γ is the compression exponent, and g_{∞} is the baseline value.[28] We found g_{∞} to be approximately 1 for all g_2s where the full decay was within the accessible time-range, indicating that the system is ergodic. Even after gelation and vitrification, a full decay of g_2 to 1 was observed, consistent with previous works on glassy soft materials.[29−31] In several cases where the full decay was not within the accessible time range, g_{∞} was set to 1 for fitting. All correlation functions showed a plateau at $\beta \approx 0.08$ for short delay times τ (unless the beginning of the relaxation was out of the accessible time-range), and the same value for β was found for a static calibration sample, indicating that there was no faster relaxation mode occurring outside our τ range. For all samples, selected g_2 fits at $q = 0.011$ Å^{-1} at various cure times are shown in Figure S4 (15−20 g_2 fits per sample). Additionally, example fits of g_2 at 10 values of q are shown in Figure S5. The q-dependence of Γ for each data set was obtained by fitting with the following function

$$\Gamma(q) = \Gamma_0 q^p \quad (2)$$

where Γ_0 is a pre-factor and p is the scaling exponent. For Brownian diffusion, $p = 2$, and for ballistic relaxations, $p = 1$.[20] At very short cure times, the fit to eq 2 was not performed because the relaxation was too fast to obtain Γ for enough q values. All fitting was done in Python using the SciPy curve_fit function[32] and the LMFIT package.[33] For all samples, selected fits of $\Gamma(q)$ at various cure times are shown in Figure S6.

Calculation of Viscosity from XPCS Data. The following two approaches were used to obtain the viscosity from XPCS data shown in Figure 4. For frequencies of 750 Hz or less, the Eiger 4M detector was used, and the signal-to-noise of the g_2 curves was high enough to use Mason's approach to obtain the complex viscosity, $|\eta^*(\omega)|$, from g_2 as[34]

$$|\eta^*(\omega)| = \frac{1}{\omega}|G^*| \approx \frac{1}{\omega} \frac{k_B T}{\pi a \langle \Delta r^2(\omega^{-1})\rangle \Gamma_f(1 + \alpha(\omega))} \quad (3)$$

where

$$\alpha(\omega) = \left.\frac{\mathrm{d} \ln\langle \Delta r^2(\tau)\rangle}{\mathrm{d} \ln \tau}\right|_{\tau=\omega^{-1}}$$

ω is the frequency (equal to τ^{-1}), k_B is the Boltzmann constant, T is the temperature, a is the NP radius, $\langle \Delta r^2(\tau)\rangle$ is the mean-squared displacement, and Γ_f is the gamma function (not to be confused with the relaxation rate, Γ). For this calculation, $\langle \Delta r^2(\tau)\rangle$ was obtained directly from g_2[35]

$$g_2(\tau) = 1 + \beta \exp[-q^2\langle \Delta r^2(\tau)\rangle/3] \quad (4)$$

Equation 4 was applied to the regions of the g_2 curves where $0.15\beta < g_2 - 1 < 0.85\beta$. This was done for all q values between 0.007 and 0.028 Å^{-1}. From this analysis, $\alpha(\omega)$ was nearly constant over this q range and was therefore obtained by a linear fit of $\ln \langle \Delta r^2(\tau)\rangle$ versus $\ln \tau$. The viscosity plotted in Figure 4 (circles) is averaged over all τ and q values. This calculation of viscosity assumes well-dispersed NPs, and the *in situ* small-angle X-ray scattering during cure shows that this is indeed the case, because the intensity plateaus as $q \to 0$ (Figure S7).

For 9 kHz frequency data, the Eiger 500k detector was used, and the signal-to-noise was significantly reduced because the smaller detector area limited the available range of azimuthal angles. With the reduced signal, we simplify the viscosity calculation by assuming Newtonian behavior, which is appropriate for early cure times when the molecular weight is low. The viscosity was calculated from this approximation of eq 3

$$|\eta^*| \approx \frac{1}{\Gamma(q)} \frac{k_B T q^2}{6\pi a} \quad (5)$$

where $\Gamma(q)$ is obtained from fitting g_2 to eq 1 (plus signs in Figure 4).

Differential Scanning Calorimetry. Differential scanning calorimetry (DSC) was performed on a DSC2500 (TA Instruments) using Tzero hermetic pans (TA Instruments). Each sample was cooled from room temperature to −80 °C at a rate of 10°C/min and then heated to 110 °C at a rate of 5 °C/min. Samples were then cured at 110 °C for 180 min while modulating the temperature with an amplitude of 0.5 °C and a period of 1 min. To obtain the enthalpy of reaction, heat flow curves were integrated with respect to time during the heating step and the isothermal step. Approximately 5% of the reaction occurred during the heating step. To convert enthalpy to degree of cure, the molar enthalpy of reaction was used, as obtained from FTIR spectra (below).

Fourier Transform Infrared Spectroscopy. FTIR spectroscopy was performed (1) to evaluate the reactivity ratio of primary versus secondary amines and (2) to obtain the molar enthalpy of reaction in conjunction with DSC. FTIR analysis was performed on a Nicolet 6700 (Thermo Scientific) equipped with a Simplex HT-32 High Temperature Transmission cell (Simplex Scientific) under nitrogen. Spectra were obtained in a wavenumber range of 2100 to 7400 cm^{-1}, with a resolution of 4 cm^{-1}. Select spectral regions are shown in Figure S8a−c. Each sample was loaded onto a glass cover slip and another glass cover slip was placed on top, using a 0.5 mm thick silicone sheet with a 1-cm circle punched out as a spacer. This assembly was placed in the simplex cell, which was heated to 110 °C at a ramp rate of 5 °C/min. Data were collected over the course of 3 h at 110 °C. The sample was then heated to 200 °C and annealed for 30 min to complete the reaction and cooled back to 110 °C for final data collection. For fitting, the final spectrum was subtracted from each spectrum, and peaks were fit with Gaussian lineshapes. The peak area (normalized to the peak area at time zero) was assumed to be

https://doi.org/10.1021/acs.macromol.1c00727
Macromolecules 2021, 54, 6575−6584

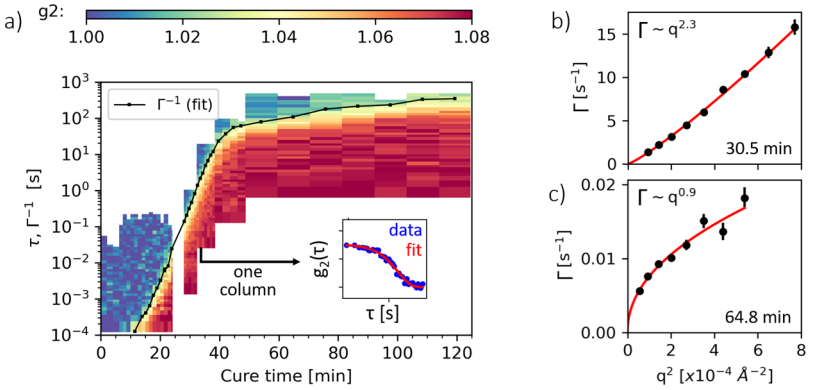

Figure 2. XPCS results for ptol-75% cured at 110 °C, shown as a representative data set. (a) Heatmap of g_2 as a function of cure time and τ at q = 0.011 Å^{-1}. The black points are the relaxation times, Γ^{-1}, obtained from fitting these g_2 curves to eq 1. Inset: the g_2 curve represented by one column is plotted in blue, and the fit to eq 1 is shown in red. (b) Relaxation rate, Γ, vs q^2 (black circles) for ptol-75% at a cure time of 30.5 min. The error bars represent the standard deviations of the fits to eq 1. A fit to eq 2, plotted in red, yields a scaling exponent of 2.3. (c) Relaxation rate *vs* q^2 at a cure time of 64.8 min, where the scaling exponent is 0.9.

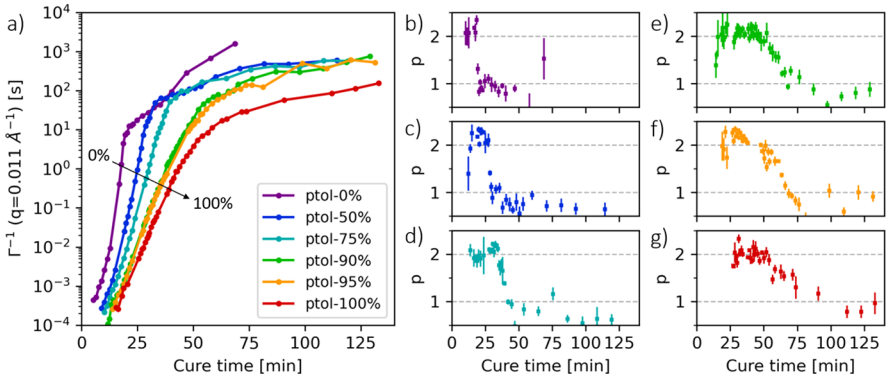

Figure 3. XPCS results for all samples cured at 110 °C: (a) Relaxation time, Γ^{-1}, at q = 0.011 Å^{-1} vs cure time and (b–g) scaling exponent of Γ with respect to q. The error bars represent the standard errors from the fits.

proportional to the population of the corresponding species (Figure S8d).

To evaluate the reactivity ratio of primary versus secondary amines, the populations of epoxy, primary amine, secondary amine, and tertiary amine as a function of cure time were obtained from the peak absorbances. Using a literature procedure,[36] we find the ratio of the rate constants, k_{NH2}/k_{NH}, to be 1.8. This assumes that k_{NH2}/k_{NH} is constant during the curing process. See Figure S8e for details.

To obtain the molar enthalpy of the reaction, the enthalpy of the reaction from the isothermal DSC experiments was used. However, to account for the incomplete reaction during the 3-h isothermal cure at 110 °C, we used FTIR to quantify the extent of reaction and rescaled the DSC enthalpy accordingly. The resulting enthalpies of reaction were 94.7 kJ/mol (ptol-0%) and 98.8 kJ/mol (ptol-100%). These enthalpies are within ≈5% of values previously reported in the literature.[24]

NMR Spectroscopy. ^{1}H NMR spectroscopy was performed before and after mixing the EPON826 nanocomposite with the curing agents to quantify the extent of reaction that occurred during the mixing process. NMR analysis was performed on a Bruker Avance operating at 400 MHz, and the resins were dissolved in *d*-chloroform. Negligible reaction occurred during these mixing steps, as shown in Figure S2.

Thermogravimetric Analysis. Thermogravimetric analysis (TGA) was performed on a Q5000 (TA Instruments) to measure the NP loading. 40 mg of ptol-0% was loaded into a platinum TGA pan and heated in air from room temperature to 600 °C at a rate of 20 °C/min, followed by an isothermal hold at 600 °C for 30 min. The final weight was 1.6% of the original weight, implying a volumetric NP loading of 0.9 vol %. In this work, we refer to the loading at 1 vol % for simplicity. An equivalent resin without NPs was measured, and its weight declined to zero (±0.02%).

Parallel Plate Rheology. Parallel plate bulk rheology was performed on an ARES-G2 rheometer (TA Instruments). 25 mm diameter plates were used for all samples except for ptol-0%, where 8 mm plates were used due to the higher viscosity and modulus. Each sample was loaded onto the lower plate with a spatula; the upper plate was lowered to a gap between 0.5 and 0.7 mm, and the material was heated from room temperature to 110 °C at a rate of 5 °C/min under flowing nitrogen. Upon reaching 110 °C, oscillatory shear rheology was performed during isothermal cure at 110 °C. The multiwave setting was used, which superimposes five oscillatory frequencies (1, 2, 4, 8, and 16 Hz). The strain of each frequency was 0.1%, resulting in a peak strain of 0.31%.

MC Simulations. Monte Carlo (MC) simulations were done using simple models of the epoxy resins as described below. Each simulation began with 10,000 DGEBPA monomers and a stoichiometric number of DDM and/or ptol monomers, depending on the sample composition. In these simulations, the monomers have no spatial dimensions or positions. In each simulation step, a random unreacted epoxide ring was bonded to a random unreacted amine proton. The probability of reaction of an amine proton was weighted by the reactivity ratio of primary versus secondary amines, which is equal to 1.8 (Figure S8e). The simulation was run until all epoxide rings and amine protons were bonded. The molecular weight distribution was calculated every 50 steps. For each composition, 20 simulations were run, and the results were averaged. The gel point was obtained from the peak in the reduced degree of polymerization (defined as the weight-average molecular weight not including the largest molecule in the system),[37] as shown in Figure S9.

https://doi.org/10.1021/acs.macromol.1c00727
Macromolecules 2021, 54, 6575−6584

RESULTS AND DISCUSSION

Relaxation Time and Its *q*-Dependence. Epoxy nanocomposites were cured at 110 °C while performing XPCS to track the NP dynamics. In Figure 2a, g_2 is plotted as a heat map for ptol-75%, a representative sample, at $q = 0.011$ Å^{-1}. This q value corresponds to a length scale of 57 nm or about four NP diameters. Each column in Figure 2a is a g_2 versus τ curve. The accessible range of τ depends upon the frame rate of the data collection, so the "steps" in the filled area correspond to changes in the frame rate. The frame rate was progressively reduced to capture the NP relaxation as it slowed by a factor of $>10^6$. The missing data at ≈25 min are where the Eiger 500k detector was exchanged for the Eiger 4M (see the Materials and Methods section). In this heat map, the relaxation time is in yellow-green color ($g_2 = 1+\beta/e \approx 1.03$). It increases rapidly until about 40 min of cure, at which time it continues to increase slowly. Overlayed on the heat map in black are the relaxation times, Γ^{-1}, obtained from fitting each of the g_2 curves to eq 1.

The scaling behavior of Γ with respect to q reveals the nature of the NP relaxation—diffusive (Brownian), subdiffusive, or hyperdiffusive—and is therefore critical to understanding the behavior of the material. In Figure 2b,c, the relaxation rate, Γ, is plotted versus q^2 at cure times of 30.5 and 64.8 min, respectively. The scaling exponent, p, is obtained by fitting these data to eq 2, and the fits are shown in red. These plots show that the scaling behavior changes dramatically during the curing process, as discussed below.

The relaxation times of each of the six samples, obtained by fitting the g_2 curves, are plotted in Figure 3a as a function of cure time. At the beginning of the cure, relaxation times were too fast to be detected, and the speckle patterns were entirely uncorrelated. At early cure times, the relaxation time increases rapidly as polymerization takes place. A higher ptol % translates to a slower increase because fewer crosslinking groups lead to a slower rise in molecular weight (Figure S10 quantifies the rate of increase for each sample). In all samples, at long cure times, there is a near-plateau in the relaxation time. This near-plateau is reached abruptly for samples with a low ptol % but gradually for samples with a high ptol %.

In Figure 3b–g, the scaling exponent of Γ with respect to q, called p (eq 2), is shown for each of the six samples. p reflects the nature of the NP relaxation: a diffusive relaxation yields $p = 2$, while a ballistic relaxation yields $p = 1$. For all samples at short cure times, $p \approx 2$, implying diffusive motion, which is expected for NPs in a Newtonian matrix. The data are noisy at short times due to the exceedingly high frame rate of 9 kHz. As the cure proceeds, p reaches values slightly above 2 for all samples. In the range of cure times where $p > 2$, α and γ are less than 1 (Figure S11), which is consistent with classical subdiffusive dynamics. According to the microrheology theory presented by Mason,[34] this subdiffusive behavior can be explained by the influence of a viscoelastic (*i.e.*, non-Newtonian) matrix. We use Mason's theory (eq 3) to calculate the complex viscosity $|\eta^*|$ (see the Materials and Methods section). Because $|\eta^*|$ is weakly frequency-dependent in the accessible range, we report $|\eta^*|$ averaged over all accessible frequencies in Figure 4. At longer times, when $p < 2$, we do not calculate $|\eta^*|$ because the above microrheology framework does not account for hyperdiffusive relaxations.

For all samples, a distinct transition occurs in which p decreases to ≈1, which indicates hyperdiffusive dynamics. At the transition time, γ increases—also consistent with hyperdiffusion (Figure S11). The highly crosslinked samples, ptol-0%, ptol-50%, and ptol-75%, exhibit a more abrupt transition in p, and this transition corresponds to the change in the slope of $\log(\Gamma^{-1})$ observed in Figure 3a. The samples with a higher ptol % exhibit a more gradual transition in p, which is concomitant with a more gradual reduction in the slope of $\log(\Gamma^{-1})$. The implications of this transition are discussed below.

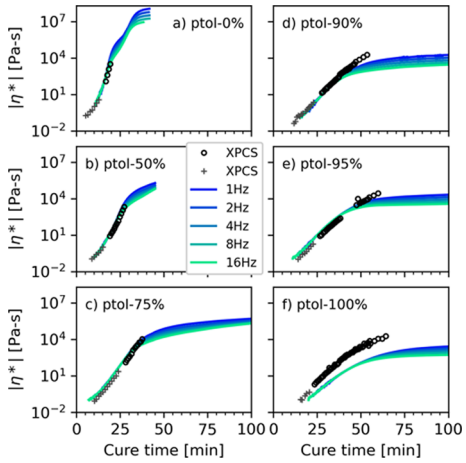

Figure 4. Viscosity, $|\eta^*|$, obtained from parallel-plate rheology at five frequencies (colored lines) and from XPCS (open circles and plus signs). The plus signs (9 kHz frame rate) were calculated *via* eq 5, while the open circles (≤750 Hz frame rate) were calculated *via* eq 3. See the Materials and Methods section for details. The six samples are plotted in (a–f) as labeled.

Bulk Rheology. To compare the nanoscale dynamics probed by XPCS with the macroscale, bulk multi-wave rheology is performed on the six samples during the cure. The complex viscosity, $|\eta^*|$, is obtained from the XPCS data via eqs 3 and 5. The result is plotted in Figure 4 and is compared with $|\eta^*|$ at the five frequencies measured by the bulk rheology. Excellent agreement—approximately within a factor of 2 throughout an ∼4 order of magnitude increase—between XPCS and rheology is observed, validating the XPCS results. The trends over time are essentially the same. Bulk rheology shows that the viscosity is frequency-independent at short cure times when the resin is a simple Newtonian liquid and becomes frequency-dependent at later times because significant polymerization makes the resin viscoelastic. When the viscosity becomes frequency-dependent, the XPCS viscosity diverges from the rheology, which is expected because the frequencies probed by XPCS are not necessarily the same as rheology (this is most clearly seen in Figure 4d,e).

Unlike the other five samples, XPCS and bulk rheology do not compare as favorably for ptol-100%. One plausible explanation is that a small amount of ptol evaporated during the bulk rheology experiment as the edges of the sample were exposed to hot, rapidly flowing nitrogen gas. This would reduce the molecular weight and therefore reduce the viscosity. For the XPCS experiments, all samples were sealed tightly with O-rings, preventing evaporation. Similarly, the samples were sealed for DSC and FTIR experiments. The DSC curing experiment for ptol-100% was repeated with a pinhole in the lid of the hermetic pan, and the enthalpy of reaction decreased by about 5%, indicating evaporation of ptol. However, the conditions in the DSC pan are not comparable to the parallel

https://doi.org/10.1021/acs.macromol.1c00727
Macromolecules 2021, 54, 6575–6584

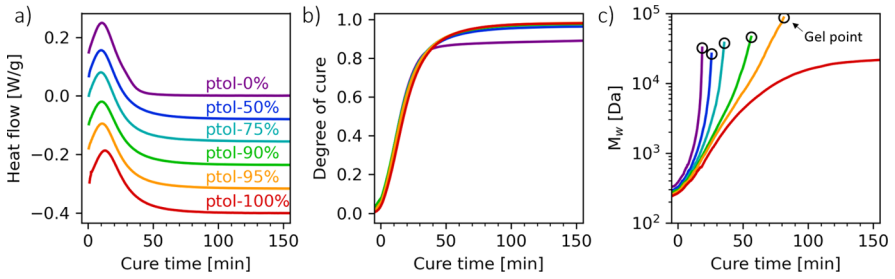

Figure 5. Cure kinetics of the six samples at 110 °C. (a) Heat flow vs cure time, as measured by DSC. The curves are offset for clarity. (b) Degree of cure vs cure time obtained from (a) and FTIR data (see the Materials and Methods section). (c) Weight-average molecular weight, M_w, from MC simulations. The simulations provide M_w as a function of degree of cure, which was translated into cure time using the data in (b). M_w is only plotted up to the gel points of the simulations, which is indicated by the black circles.

plates, so we cannot use the DSC result to quantify the amount of evaporation in the bulk rheology experiment.

Cure Kinetics. For a thorough understanding of the dynamic evolution of these systems, the degree of cure and molecular weight must be understood as a function of cure time. DSC and *in situ* FTIR are coupled with MC simulations to characterize cure kinetics, molecular weight evolution, and gelation.

The reaction kinetics of the six samples are alike. The DSC heat flows of the six samples are plotted in Figure 5a. The peaks in the heat flow occur between 10 and 13 min. Notably, the reaction of ptol-0% is mostly arrested after about 45 min, while the other samples show a gradual slowing of the reaction. This is because ptol-0% undergoes a glass transition during cure at 110 °C: its T_g is 136 °C after curing at 110 °C for 3 h (Figure S12). For all samples, the heat flow is converted to degree of cure in Figure 5b (see the Materials and Methods section). The cure time is defined as zero when the curing temperature is reached; a small amount (≈5%) of the reaction occurs prior to this, during the heating ramp. ptol-0% reaches a lower degree of cure than the other samples due to its glass transition.

MC simulations of the curing reactions were performed to estimate the gel point and the molecular weight distribution as a function of degree of cure for the six samples. Each simulation began with a stoichiometric proportion of epoxy monomers and amine monomers and one at a time, a random free epoxide ring and a random free amine proton were bonded together to simulate the cure reaction. These mean field simulations do not account for spatial or steric effects as the monomers are not assigned positions in space. The simulations account for the difference in reactivity of primary and secondary amines, so the gel points are slightly higher than those predicted by Flory−Stockmayer theory.[38,39]

The weight-average molecular weight, M_w, from the simulations is plotted in Figure 5c, where the degree of cure was translated to cure time using the curves in Figure 5b. As expected, the simulations predict that increasing the ptol % reduces the M_w of the system at a given cure time. ptol-0%, ptol-50%, and ptol-75% have superexponential growth of M_w up to the gel point. In ptol-90% and ptol-95%, M_w starts to level off at about 35 and 50 min, respectively, due to slowing of the reaction rate. Then, M_w growth accelerates again as the systems approach gelation. ptol-100% is a linear polymer, so M_w plateaus as the reaction slows. It should be noted that the final M_w of ptol-100% in Figure 5c has a significant uncertainty because it is sensitive to small errors in the final degree of cure.

Dependence of Viscosity on Molecular Weight. With the results from DSC, FTIR, and MC simulations, $|\eta^*|$ can be plotted as a function of simulated M_w for the six samples (Figure 6). It is now clear that for low M_w (<10^3 Da), $|\eta^*|$ depends primarily on M_w regardless of the sample composition. ptol-100% forms linear chains, and as its M_w increases, $|\eta^*|$ continues to increase with a similar power law. For the other samples, as M_w increases beyond several kDa, a lower ptol % results in a lower viscosity. At constant M_w, the key difference between the samples is that a lower ptol % (*i.e.*, higher DDM content) leads to more branching and higher molecular weight dispersity. These results suggest that in this epoxy system, increased branching and dispersity serve to reduce the viscosity at a given M_w. Increased branching reduces the hydrodynamic volume of the chains,[40] which could be the reason for the lower viscosity.

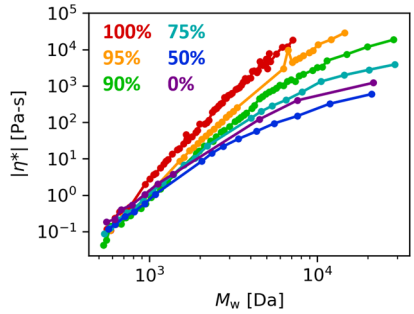

Figure 6. Viscosity from XPCS plotted as a function of weight-average molecular weight (M_w) for the six samples prior to gelation. The cure times were converted to M_w using the data in Figure 5b,c. Data points are excluded from the plot if p < 2 or if the degree of cure surpasses the theoretical gel point.

Gelation, Entanglement, and Vitrification. Does vitrification play a role in the transition of p from 2 to 1? Only ptol-0% and ptol-50% vitrify during cure at 110 °C (Figure S12), and for those samples, vitrification occurs at ≈30 and ≈100 min, respectively (Figure S13), after gelation and after the transition of p. Figure 7a shows p from XPCS and Figure 7b shows G′ and G″ from bulk rheology during cure for ptol-0%. Gelation, as indicated by the crossing of G′ and G″, occurs at precisely the same time as the sharp transition in p. Clearly, the transition in p is due to gelation for ptol-0%. Figure 7c shows the reversing heat capacity $C_{p,r}$ (from modulated DSC), which declines upon vitrification. A second transition in the bulk rheology occurs simultaneously with the decline in $C_{p,r}$, at about 30 min, signaling the glass transition.

https://doi.org/10.1021/acs.macromol.1c00727
Macromolecules 2021, 54, 6575−6584

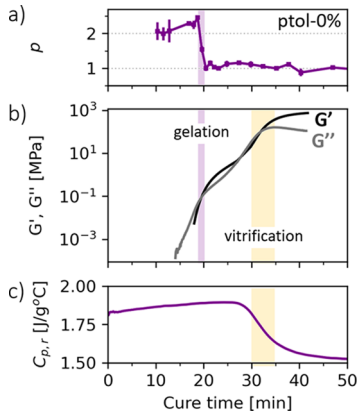

Figure 7. Comparison of transitions in ptol-0% during 110 °C cure: (a) scaling exponent p, from XPCS; (b) storage (G′) and loss (G″) moduli at 2 Hz, from bulk rheology; and (c) reversing heat capacity, from modulated DSC.

After the material becomes glassy, G′ reaches 10^3 Pa s and G′ ≫ G″. The glass transition has negligible influence on p. However, it does cause the NP relaxation to become even slower—in Figure 3a, the slope of Γ^{-1} increases at about 30 min, eventually approaching a relaxation time of 10^3 seconds at $q = 0.011$ Å^{-1}.

With the knowledge of the gelation and vitrification transitions in ptol-0%, we now examine gelation in the other five samples. p is plotted in Figure 8 along with the times at

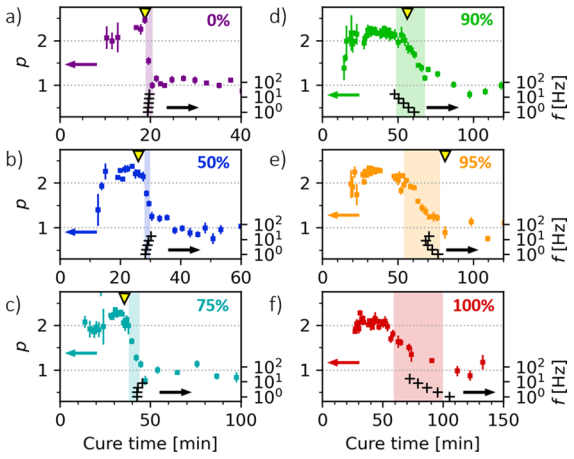

Figure 8. For each of the six samples (a–f, as indicated), the evolution of p is plotted against cure time (squares). Also shown are the times at which G′ surpasses G″ for five frequencies, as obtained from bulk multiwave rheology (black plus signs). The gel point predictions, from MC simulations, are indicated by the yellow triangles. The transition regions are shaded for clarity. Note the different limits of the x axes.

which G′ surpasses G″ from bulk rheology at each of the five frequencies measured (black plus signs). ptol-0%, ptol-50%, and ptol-75% show an abrupt transition in p, and the G′ G″ crossing point is nearly frequency-independent. This classical rheological signature of gelation[41] coincides with the transition in p, leading to the conclusion that the p transition is simply due to gelation in these three samples. MC simulation predictions of gelation times, indicated by yellow triangles, also agree with the transitions in p. (ptol-50% vitrification occurs at much later cure times, see Figure S13.) $p = 1$ after gelation is consistent with previous reports of hyperdiffusive dynamics in gelled systems, such as grafted NPs in solvents,[42,43] polymer clusters in water,[44] and polymer NPs in aqueous solution.[45] The $p = 1$ scaling is frequently attributed to stress relaxation processes.

The remaining samples—ptol-90%, ptol-95%, and ptol-100%—tell a different story. Here, the transition in p is gradual and the G′/G″ crossing point is highly frequency-dependent. ptol-100% forms a linear polymer, and yet the signatures of network formation are still present. This can be explained in the context of prior work on polymer nanocomposites. Mangal *et al.* found that when the polymer matrix molecular weight is below its entanglement molecular weight M_e, the NP dynamics are diffusive ($p = 2$),[46] but when the matrix molecular weight was greater than M_e, the NP dynamics were hyperdiffusive ($p \approx 1$). While the M_e of the linear polymer formed by ptol-100% is not known, it is reasonable to assume that the transition in p is due to the formation of an entanglement network. As seen in Figure 5c, simulations predict that at the time of its transition in p, ptol-100% has M_w of the order 10^4 Da, a reasonable value for M_e.[47] In the bulk rheology data, the highly frequency-dependent crossing of G′ and G″ is also consistent with the formation of an entanglement network, and the post-cure time–temperature superposition plot confirms the presence of an entanglement network (Figure S14) (the sample in Figure S14 was cured in a sealed vial to prevent evaporation of ptol). It should be noted that while etherification reactions are possible in ptol-100%, leading to branching and crosslinking, the rate of etherification is negligible at 110 °C.[48] Furthermore, Figure S14 shows no evidence of crosslinking in ptol-100%.

Are the p transitions in ptol-90% and ptol-95% governed by entanglements or by gelation? In ptol-95%, the gel point predicted by MC simulation (yellow triangle) occurs long after the onset of the p transition, and the M_w at the time of the p transition is ∼10^4 Da. A ptol-95% chain with a molecular weight of 10^4 Da is expected to be mostly linear, having on average 0.6 DDM monomers per chain. These facts seem to point toward entanglement as contributing to ptol-95%'s transition. However, we cannot rule out a gelation process that is more gradual than assumed by our simple MC simulations. If gelation is spatially heterogeneous, as proposed in other works,[11,15−17] the onset of the gelation-driven p transition may occur sooner than the simulations predict. The gradual decline of p might reflect the slow spreading of the gelled region. Future studies, where the NP size is varied, will determine whether this is the case. Meanwhile, ptol-90% (Figure 8d) bears some similarities to ptol-95% (Figure 8e), except that the onset of the p transition is well-predicted by the MC simulations. The data suggest that for ptol-90%, the p transition is the result of a complex interplay between chemical gelation, entanglement network formation, and perhaps spatial heterogeneity of crosslink density. In this sample, the contributions of these three phenomena cannot be disentangled without further study.

It is important to stress that the abrupt transition in p observed in ptol-0%, ptol-50%, and ptol-75% is inconsistent with crosslink heterogeneity on 10s to 1000s of nanometer length scales, as was suggested in previous studies of other epoxy resins.[11−17] Since XPCS samples nanoscale dynamics over bulk volumes of material (here >10^6 μm^3), it would detect a two-phase system with two effective matrix conditions. Presumably, the two phases would gel at different times. We observe an abrupt transition in p for the three samples with

https://doi.org/10.1021/acs.macromol.1c00727
Macromolecules 2021, 54, 6575−6584

lower ptol %, indicating that the entire material gels nearly at once. On the other hand, if the length scale of heterogeneity is small, such that the NPs span multiple domains, these experiments would not capture it. Also, it is not impossible that the NPs themselves influence the crosslink heterogeneity, but one might expect a major influence on the curing process to change the bulk rheology. In Figure S15, the bulk rheology curves of ptol-0% with and without NPs are similar, aside from a moderate increase of the reaction rate caused by the NPs (see DSC result, Figure S16). Future work should investigate other industrial epoxy systems using XPCS to further evaluate the hypothesis of crosslink heterogeneity in these materials.

CONCLUSIONS

The curing processes of six epoxy nanocomposites were examined *via* XPCS. Two amine curing agents were used in varying ratios such that the resins ranged from a traditional epoxy formulation (100% DDM, a difunctional amine) to a linear polymer (100% ptol, a monofunctional amine). Using XPCS, we tracked the dynamics of the silica NPs as the associated timescales slowed by a factor of $>10^6$ during cure. Prior to network formation, the NPs were diffusive or moderately subdiffusive, and the viscosities obtained from XPCS were consistent with bulk rheology. At a given M_w during cure, samples with higher DDM content had lower zero-shear viscosity, suggesting that increased branching and/or higher M_w dispersity cause lower viscosity in this system.

All six samples showed a pronounced transition of the scaling exponent p, decreasing from $\gtrsim 2$ to ≈ 1. For the samples with higher DDM content (ptol-0%, ptol-50%, and ptol-75%), the transition was abrupt and corresponded to gelation of the crosslink network. The abruptness of the transition suggested that the entire material gels nearly at once and that crosslink heterogeneity is not present at length scales larger than the NP size (15 nm) and smaller than the sampled volume (10^6 μm^3). For ptol-100%, the transition was gradual and most likely corresponded to the formation of an entanglement network. ptol-90% and ptol-95% closely resembled ptol-100% but their transitions were more complex. They were likely caused by a combination of the entanglement and gelation processes.

This work presents a unique study that uses XPCS to address fundamental questions about the curing process of epoxy resins. Efforts are underway to replace the silica NPs with heavy-metal NPs. This will dramatically improve the signal due to enhanced electron density contrast and allow tunable NP size. With an improved signal, even more information could be extracted from the data, such as the q-dependence of γ and a direct measurement of dynamical heterogeneities through 4-point correlation functions.[45] Furthermore, by varying the NP size, the effect on the microrheology and the p transition will be understood, thereby probing the length scale of the network.

Insights from these studies will aid mesoscale modeling of thermoset curing for industrially relevant resin formulations. These modeling efforts rely on experimental verifications which are currently limited to FTIR and other spectroscopy methods with no local dynamics and morphological information. Combined with mesoscale modeling,[10] cure cycle optimization could take a step further toward becoming a more physics-based process. Missing input parameters for mesoscale modeling, such as diffusion coefficients of NPs, allows the modeling community to improve cure cycles digitally rather than by trial and error while maintaining the mechanical performance. Finally, the results reported here will enable future in situ studies of thermoset polymerization and gelation in industrial parts where bulk rheology is impractical.

ASSOCIATED CONTENT

Supporting Information

The Supporting Information is available free of charge at https://pubs.acs.org/doi/10.1021/acs.macromol.1c00727.

Small-angle X-ray scattering, NMR, additional XPCS data and analysis, FTIR, MC simulations, DSC, and rheology results (PDF)

AUTHOR INFORMATION

Corresponding Author

Hilmar Koerner − *Materials & Manufacturing Directorate, Air Force Research Laboratory, WPAFB, Ohio 45433, United States;* orcid.org/0000-0002-1864-8193; Email: hilmar.koerner.1@us.af.mil

Authors

Edward B. Trigg − *Materials & Manufacturing Directorate, Air Force Research Laboratory, WPAFB, Ohio 45433, United States; UES, Inc., Dayton, Ohio 45432, United States;* orcid.org/0000-0002-4723-650X

Lutz Wiegart − *National Synchrotron Light Source II, Brookhaven National Laboratory, New York 11973, United States;* orcid.org/0000-0003-4417-8479

Andrei Fluerasu − *National Synchrotron Light Source II, Brookhaven National Laboratory, New York 11973, United States*

Complete contact information is available at: https://pubs.acs.org/10.1021/acs.macromol.1c00727

Author Contributions

E.B.T. designed and carried out experiments, performed the analysis, and wrote the manuscript. E.B.T. and H.K. conceived of the project, and H.K. supervised the project. L.W. and A.F. provided guidance for XPCS experiments and analysis, provided code for data analysis, and executed some XPCS experiments. All authors contributed to editing and have approved of the final version of the manuscript.

Funding

This research was performed in part while E.B.T. held an NRC Research Associateship award at the Air Force Research Laboratory. This research used beamline 11-ID (CHX) of the National Synchrotron Light Source II, a U.S. Department of Energy (DOE) Office of Science User Facility operated for the DOE Office of Science by Brookhaven National Laboratory under Contract No. DE-SC0012704. H.K. acknowledges support from the Air Force Office of Scientific Research (J. Tiley, M.-J. Pan) under the Low Density Portfolio #17RXCOR436.

Notes

The authors declare no competing financial interest.

ACKNOWLEDGMENTS

We thank Dr. Eric Bailey (DuPont) for helpful discussions.

REFERENCES

(1) Min, B.-G.; Hodgkin, J. H.; Stachurski, Z. H. The Dependence of Fracture Properties on Cure Temperature in a DGEBA/DDS Epoxy System. *J. Appl. Polym. Sci.* **1993**, *48*, 1303−1312.

(2) Sharifi, M.; Jang, C. W.; Abrams, C. F.; Palmese, G. R. Toughened Epoxy Polymers via Rearrangement of Network Topology. *J. Mater. Chem. A* **2014**, *2*, 16071−16082.
(3) Araki, W.; Adachi, T.; Yamaji, A.; Gamou, M. Fracture Toughness of Bisphenol A-Type Epoxy Resin. *J. Appl. Polym. Sci.* **2002**, *86*, 2266−2271.
(4) Araki, W.; Adachi, T.; Gamou, M.; Yamaji, A. Time-Temperature Dependence of Fracture Toughness for Bisphenol a Epoxy Resin. *Proc. Inst. Mech. Eng., Part L* **2002**, *216*, 79−84.
(5) Lascano, D.; Quiles-Carrillo, L.; Torres-Giner, S.; Boronat, T.; Montanes, N. Optimization of the Curing and Post-Curing Conditions for the Manufacturing of Partially Bio-Based Epoxy Resins with Improved Toughness. *Polymers* **2019**, *11*, 1354.
(6) Meyer, F.; Sanz, G.; Eceiza, A.; Mondragon, I.; Mijović, J. The Effect of Stoichiometry and Thermal History during Cure on Structure and Properties of Epoxy Networks. *Polymer* **1995**, *36*, 1407−1414.
(7) Zhavoronok, E. S.; Senchikhin, I. N.; Roldughin, V. I. Physical Aging and Relaxation Processes in Epoxy Systems. *Polym. Sci., Ser. A* **2017**, *59*, 159−192.
(8) Ellis, B. The Kinetics of Cure and Network Formation. In *Chemistry and Technology of Epoxy Resins*; Ellis, B., Ed.; Springer Netherlands: Dordrecht, 1993; pp 72−116.
(9) Schlosser, E.; Schönhals, A. Recent Development in Dielectric Relaxation Spectroscopy of Polymers. *Colloid Polym. Sci.* **1989**, *267*, 963−969.
(10) Estridge, C. E. The Effects of Competitive Primary and Secondary Amine Reactivity on the Structural Evolution and Properties of an Epoxy Thermoset Resin during Cure: A Molecular Dynamics Study. *Polymer* **2018**, *141*, 12−20.
(11) Bahrami, A.; Morelle, X.; Hông Minh, L. D.; Pardoen, T.; Bailly, C.; Nysten, B. Curing Dependent Spatial Heterogeneity of Mechanical Response in Epoxy Resins Revealed by Atomic Force Microscopy. *Polymer* **2015**, *68*, 1−10.
(12) Sahagun, C. M.; Morgan, S. E. Thermal Control of Nanostructure and Molecular Network Development in Epoxy-Amine Thermosets. *ACS Appl. Mater. Interfaces* **2012**, *4*, 564−572.
(13) Gu, X.; Raghavan, D.; Ho, D. L.; Sung, L.; VanLandingham, M. R.; Nguyen, T. Nanocharacterization of Surface and Interface of Different Epoxy Networks. *Mater. Res. Soc. Symp. Proc.* **2002**, *710*, 153−158.
(14) Kishi, H.; Naitou, T.; Matsuda, S.; Murakami, A.; Muraji, Y.; Nakagawa, Y. Mechanical Properties and Inhomogeneous Nanostructures of Dicyandiamide-Cured Epoxy Resins. *J. Polym. Sci., Part B: Polym. Phys.* **2007**, *45*, 1425−1434.
(15) Morsch, S.; Liu, Y.; Lyon, S. B.; Gibbon, S. R. Insights into Epoxy Network Nanostructural Heterogeneity Using AFM-IR. *ACS Appl. Mater. Interfaces* **2016**, *8*, 959−966.
(16) Morsch, S.; Liu, Y.; Greensmith, P.; Lyon, S. B.; Gibbon, S. R. Molecularly Controlled Epoxy Network Nanostructures. *Polymer* **2017**, *108*, 146−153.
(17) Aoki, M.; Shundo, A.; Kuwahara, R.; Yamamoto, S.; Tanaka, K. Mesoscopic Heterogeneity in the Curing Process of an Epoxy-Amine System. *Macromolecules* **2019**, *52*, 2075−2082.
(18) Duchet, J.; Pascault, J. P. Do Epoxy-Amine Networks Become Inhomogeneous at the Nanometric Scale? *J. Polym. Sci., Part B: Polym. Phys.* **2003**, *41*, 2422−2432.
(19) Haba, D.; Kaufmann, J.; Brunner, A. J.; Resch, K.; Teichert, C. Observation of Elastic Modulus Inhomogeneities in Thermosetting Epoxies Using AFM—Discerning Facts and Artifacts. *Polymer* **2014**, *55*, 4032−4040.
(20) Bikondoa, O. X-Ray Photon Correlation Spectroscopy for the Characterization of Soft and Hard Condensed Matter. *X-ray and Neutron Techniques for Nanomaterials Characterization*; Springer-Verlag: Berlin Heidelberg, 2016; pp 95−156.
(21) Nogales, A.; Fluerasu, A. X Ray Photon Correlation Spectroscopy for the Study of Polymer Dynamics. *Eur. Polym. J.* **2016**, *81*, 494−504.
(22) Squires, T. M.; Mason, T. G. Fluid Mechanics of Microrheology. *Annu. Rev. Fluid. Mech.* **2010**, *42*, 413−438.
(23) Yavitt, B. M.; Salatto, D.; Huang, Z.; Koga, Y. T.; Endoh, M. K.; Wiegart, L.; Petrash, S.; Koga, T. Revealing Nanoscale Dynamics during an Epoxy Curing Reaction with X-Ray Photon Correlation Spectroscopy. *J. Appl. Phys.* **2020**, *127*, 114701.
(24) Blanco, M.; Corcuera, M. A.; Riccardi, C. C.; Mondragon, I. Mechanistic Kinetic Model of an Epoxy Resin Cured with a Mixture of Amines of Different Functionalities. *Polymer* **2005**, *46*, 7989−8000.
(25) Sutton, M.; Laaziri, K.; Livet, F.; Bley, F. Using Coherence to Measure Two-Time Correlation Functions. *Opt. Express* **2003**, *11*, 2268.
(26) Abeykoon, S. K.; Zhang, Y.; Dill, E. D.; Caswell, T. A.; Allan, D. B.; Akilic, A.; Wiegart, L.; Wilkins, S.; Heroux, A.; Kleese van Dam, K., Sutton, M.; et al. *Software Tools for X-Ray Photon Correlation and X-Ray Speckle Visibility Spectroscopy*; IEEE: United States, 2016.
(27) Williams, G.; Watts, D. C. Non-Symmetrical Dielectric Relaxation Behaviour Arising from a Simple Empirical Decay Function. *Trans. Faraday Soc.* **1970**, *66*, 80−85.
(28) Leheny, R. L. XPCS: Nanoscale Motion and Rheology. *Curr. Opin. Colloid Interface Sci.* **2012**, *17*, 3−12.
(29) Cipelletti, L.; Ramos, L.; Manley, S.; Pitard, E.; Weitz, D. A.; Pashkovski, E. E.; Johansson, M. Universal Non-Diffusive Slow Dynamics in Aging Soft Matter. *Faraday Discuss.* **2003**, *123*, 237−251.
(30) Cipelletti, L.; Manley, S.; Ball, R. C.; Weitz, D. A. Universal Aging Features in the Restructuring of Fractal Colloidal Gels. *Phys. Rev. Lett.* **2000**, *84*, 2275−2278.
(31) Kwaśniewski, P.; Fluerasu, A.; Madsen, A. Anomalous Dynamics at the Hard-Sphere Glass Transition. *Soft Matter* **2014**, *10*, 8698−8704.
(32) Virtanen, P.; Gommers, R.; Oliphant, T. E.; Haberland, M.; Reddy, T.; Cournapeau, D.; Burovski, E.; Peterson, P.; Weckesser, W.; Bright, J.; et al. SciPy 1.0: Fundamental Algorithms for Scientific Computing in Python. *Nat. Methods* **2020**, *17*, 261−272.
(33) Newville, M.; Stensitzki, T.; Allen, D. B.; Ingargiola, A. *LMFIT: Non-linear Least-Square Minimization and Curve-Fitting for Python*, version 0.8.0, 2014, https://doi-org.wrs.idm.oclc.org/10.5281/ZENODO.11813.
(34) Mason, T. G. Estimating the Viscoelastic Moduli of Complex Fluids Using the Generalized Stokes-Einstein Equation. *Rheol. Acta* **2000**, *39*, 371−378.
(35) Berne, B. J.; Pecora, R. *Dynamic Light Scattering: With Applications to Chemistry, Biology, and Physics*; John Wiley and Sons: New York, 1976.
(36) Paz-Abuin, S.; Lopez-Quintela, A.; Varela, M.; Pazos-Pellín, M.; Prendes, P. Method for Determination of the Ratio of Rate Constants, Secondary to Primary Amine, in Epoxy-Amine Systems. *Polymer* **1997**, *38*, 3117−3120.
(37) Polanowski, P.; Jeszka, J. K.; Matyjaszewski, K. Modeling of Branching and Gelation in Living Copolymerization of Monomer and Divinyl Cross-Linker Using Dynamic Lattice Liquid Model (DLL) and Flory-Stockmayer Model. *Polymer* **2010**, *51*, 6084−6092.
(38) Flory, P. *Principles of Polymer Chemistry*; Cornell University Press: Ithaca, NY, 1953.
(39) Stockmayer, W. H. Theory of Molecular Size Distribution and Gel Formation in Branched-Chain Polymers. *J. Chem. Phys.* **1944**, *12*, 125−131.
(40) Young, R. J.; Lovell, P. A. *Introduction to Polymers*, 3rd ed.; CRC Press: Boca Raton, FL, 1991.
(41) *ASTM D4473, Plastics (I), Dynamic Mechanical Properties: Cure Behavior*; ASTM: Philadelphia, 2008.
(42) Guo, H.; Ramakrishnan, S.; Harden, J. L.; Leheny, R. L. Gel Formation and Aging in Weakly Attractive Nanocolloid Suspensions at Intermediate Concentrations. *J. Chem. Phys.* **2011**, *135*, 154903.
(43) Frenzel, L.; Lehmkühler, F.; Lokteva, I.; Narayanan, S.; Sprung, M.; Grübel, G. Anomalous Dynamics of Concentrated Silica-PNIPAm Nanogels. *J. Phys. Chem. Lett.* **2019**, *10*, 5231−5236.

https://doi.org/10.1021/acs.macromol.1c00727
Macromolecules 2021, 54, 6575−6584

(44) Czakkel, O.; Madsen, A. Evolution of Dynamics and Structure during Formation of a Cross-Linked Polymer Gel. *Europhys. Lett.* **2011**, *95*, 28001.
(45) Duri, A.; Cipelletti, L. Length Scale Dependence of Dynamical Heterogeneity in a Colloidal Fractal Gel. *Europhys. Lett.* **2006**, *76*, 972−978.
(46) Mangal, R.; Srivastava, S.; Narayanan, S.; Archer, L. A. Size-Dependent Particle Dynamics in Entangled Polymer Nanocomposites. *Langmuir* **2016**, *32*, 596−603.
(47) Hiemenz, P. C.; Lodge, T. P. *Polymer Chemistry*, 2nd ed.; CRC Press: Boca Raton, FL, 2007.
(48) Xu, L.; Schlup, J. R. Etherification Versus Amine Addition During Epoxy Resin/Amine Cure: An In Situ Study Using Near-Infrared Spectroscopy. *J. Appl. Polym. Sci.* **1998**, *67*, 895−901.

https://doi.org/10.1021/acs.macromol.1c00727
Macromolecules 2021, 54, 6575−6584